

Correction of systematic spatial noise in push-broom hyperspectral sensors: application to CHRIS/PROBA images

Luis Gómez-Chova,^{1,*} Luis Alonso,² Luis Guanter,³ Gustavo Camps-Valls,¹
Javier Calpe,¹ and José Moreno²

¹Department of Electronic Engineering, University of Valencia, Dr. Moliner 50, 46100 Burjassot, Valencia, Spain

²Department of Earth Physics and Thermodynamics, University of Valencia, Dr. Moliner 50, 46100 Burjassot, Valencia, Spain

³GeoForschungsZentrum Potsdam, Remote Sensing Section, Telegrafenberg, D-14473 Potsdam, Germany

*Corresponding author: luis.gomez-chova@uv.es

Received 13 March 2008; revised 12 June 2008; accepted 12 June 2008;
posted 16 June 2008 (Doc. ID 93807); published 22 July 2008

Hyperspectral remote sensing images are affected by different types of noise. In addition to typical random noise, nonperiodic partially deterministic disturbance patterns generally appear in the data. These patterns, which are intrinsic to the image formation process, are characterized by a high degree of spatial and spectral coherence. We present a new technique that faces the problem of removing the spatially coherent noise known as vertical striping, usually found in images acquired by push-broom sensors. The developed methodology is tested on data acquired by the Compact High Resolution Imaging Spectrometer (CHRIS) onboard the Project for On-board Autonomy (PROBA) orbital platform, which is a typical example of a push-broom instrument exhibiting a relatively high noise component. The proposed correction method is based on the hypothesis that the vertical disturbance presents higher spatial frequencies than the surface radiance. A technique to exclude the contribution of the spatial high frequencies of the surface from the destriping process is introduced. First, the performance of the proposed algorithm is tested on a set of realistic synthetic images with added modeled noise in order to quantify the noise reduction and the noise estimation accuracy. Then, algorithm robustness is tested on more than 350 real CHRIS images from different sites, several acquisition modes (different spatial and spectral resolutions), and covering the full range of possible sensor temperatures. The proposed algorithm is benchmarked against the CHRIS reference algorithm. Results show excellent rejection of the noise pattern with respect to the original CHRIS images, especially improving the removal in those scenes with a natural high contrast. However, some low-frequency components still remain. In addition, the developed correction model captures and corrects the dependency of the noise patterns on sensor temperature, which confirms the robustness of the presented approach. © 2008 Optical Society of America

OCIS codes: 030.1670, 030.4280, 100.3020, 110.4234, 280.4788.

1. Introduction

Hyperspectral images acquired by remote sensing instruments are generally affected by two kinds of noise. The first one can be defined as standard random noise, which varies with time and determines the minimum image signal-to-noise ratio [1,2]. In ad-

dition, hyperspectral images can present nonperiodic partially deterministic disturbance patterns [3], which come from the image formation process and are characterized by a high degree of spatial and spectral coherence [4].

Many of the hyperspectral sensors are push-broom imaging spectrometers. Push-broom line imagers consist of an optical system that focuses the light coming from a portion of the Earth's surface onto

the focal plane where the sensor is placed. The system includes a long and narrow slit that limits the area being imaged to a stripe aligned with one of the sensor's axes, while a diffractive medium (prism, grid, etc.) forms a spectrum of the line along the orthogonal axis. Usually the detector is a charge coupled device (CCD) two-dimensional array whose rows separate wavelengths and whose columns separate resolved points in the Earth image [5]. Figure 1 shows the push-broom operation mode for the acquisition of spectral images. The optical system collects the light arriving from a long and narrow strip of the surface below by means of a thin slit. The slit is oriented perpendicularly to the direction of motion of the sensor, and the sequential acquisition of lines generates the image as the platform moves forward. The image of the land strip is diffracted, separating the different wavelengths, and projected onto a properly aligned CCD array; so the line is parallel to the horizontal axis (spatial), while the diffraction is produced along the perpendicular axis (spectral).

Summarizing, the complete optical design is optimized so that monochromatic images of the slit fall on straight CCD rows, and line spectra of resolved ground areas fall on CCD columns. In this case, each pixel in a line of the image at a given wavelength is acquired by a different element of the CCD, while every column of the image for that wavelength is measured by the same element of the CCD. Were the CCD and the slit ideally built, then all CCD elements would have the same sensitivity and response, producing even noise-free images. However, in real devices deviations from these design conditions produce undesired effects [3,6]. One of them is the variation of the intensity of a homogeneous imaged area in each column of the CCD array, which is due to sensitivity variations between neighboring elements of the CCD and variations in the width of the slit along its length [3]. The effect of these imperfections in the resulting image is a vertical pattern known as vertical striping (VS). Usually the whole system is fully characterized after assembly, yielding the gain correction factors that would produce an even image in operational situations. However, on some occasions, especially after rocket launch, the system is affected in such a way that the characterization does not completely remove the noise. Also, this type of sensor degrades with time and thus needs recalibration, which is not always possible. In those cases, a noise-reduction algorithm must be applied after image reception in the preprocessing phase.

This work analyzes the Compact High Resolution Imaging Spectrometer (CHRIS) [7], which is mounted onboard the European Space Agency (ESA) small satellite platform called PROBA (Project for On-board Autonomy) [8]. The CHRIS sensor [7] provides multiangular hyperspectral images in the spectral range from 400 to 1050 nm with a maximum spatial resolution of 17 or 34 m at nadir, depending on the acquisition mode. CHRIS has five selectable acquisition modes, which depend mainly on the band

wavelength configuration and the four possible swath width and binning options available (<http://earth.esa.int/missions/thirdpartymission/proba.html>). Currently, there are no standard processing algorithms defined for CHRIS because PROBA was originally designed as a technology demonstrator satellite and CHRIS data were a secondary objective of the mission. In fact, radiometric calibration is the only preprocessing step applied to CHRIS data before delivering image products, which are provided in top of the atmosphere radiance [9]. As a consequence, CHRIS images present a certain number of problems and errors [10] that are commonly removed from most remote sensing data.

As a push-broom sensor, the radiometric response of the CHRIS instrument is determined by two overlapping components: the optical system response (a telescope forming an image on the entrance slit together with the spectrometer) and the CCD response (a thinned, backilluminated, frame-transfer CCD) [8]. With regard to the CCD response, the different pixel-to-pixel responses come from nonuniformities in dark current generation, nonuniformities in pixel sensitivity, threshold variations, and gain and offset differences [11]. But, in practice, these CCD imperfections are relatively stable with temperature and time [12], resulting in a spatially fixed-pattern noise in the image that should be removed (e.g., the dark signal offsets are removed by subtracting a generic dark image). However, with regard to the optical system response, changes in temperature, due to the seasonal variation of the in-orbit CHRIS instrument temperature [12], produce a dilation of the slit that changes its width and moves the image of the slit across the detector. Therefore, the effect of the slit adds to the vertical pattern in a complex way, as it is heavily dependent on the sensor's temperature (see Fig. 1), and thus it must be modeled and corrected.

Several VS-reduction approaches have been proposed in the literature. Our approach falls in the category of scene-based nonuniformity corrections, since it provides relative calibration factors directly computed from the acquired image. Methods based on large uniform areas in the scene or methods assuming constant-static noise patterns [13,14] are not appropriate for CHRIS because of its spatial resolution (17 to 34 m) and its noise dependence on the sensor's temperature, respectively. Other methods assume that all sensor elements observe similar subscenes in a given image and adjust the distributions of values acquired by each sensor to some reference distribution by means of a histogram or moment matching [15], but the high spatial resolution of CHRIS and the moderate number of lines per image also dissuade us from their use. Finally, most related methods assume that the noise contribution changes from one pixel to another (high spatial frequency) in the across-track direction, while the surface contribution presents smoother profiles (lower spatial frequencies) in the across-track dimension [3,16–18].

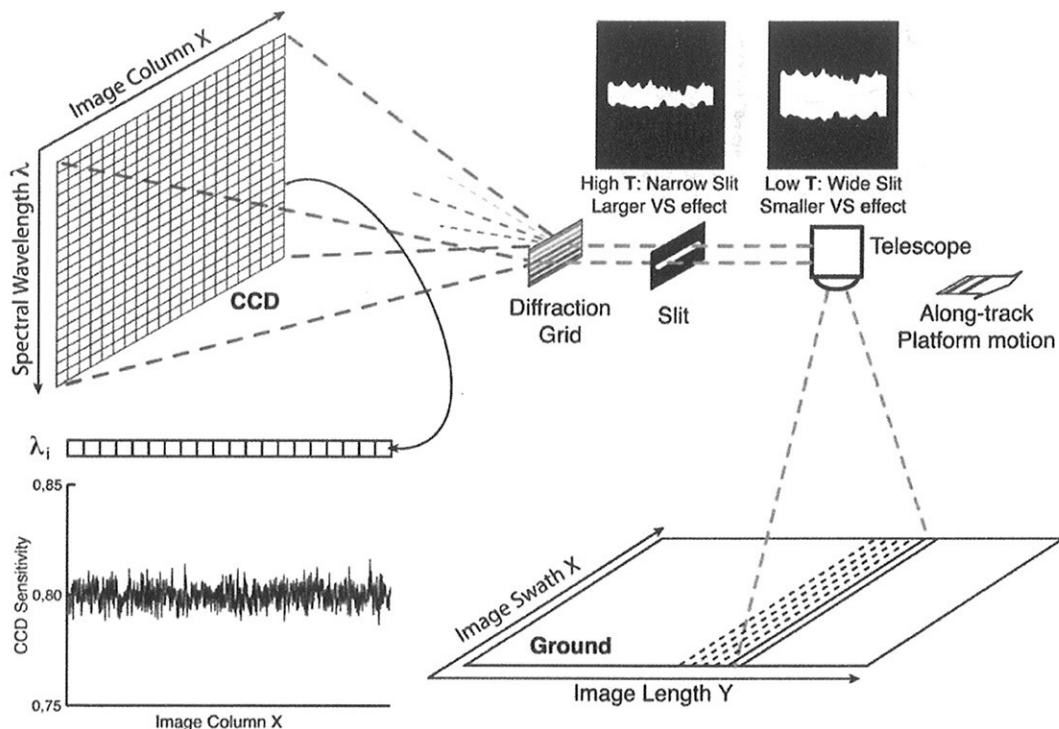


Fig. 1. (Color online) Design of a push-broom imaging spectrometer that shows its operation mode and the sources of the coherent spatial noise patterns: entrance slit width that depends on temperature (T), and CCD sensitivity (figure based on [3]).

This approach is described in more detail in Subsection 2.C, but the reader is referred to [19] for a full description of scene-based nonuniformity correction methods for push-broom sensors. One novelty of the proposed VS-correction method is that it explicitly introduces a technique for excluding the contribution of the surface's spatial high frequencies from the destriping process. The proposed approach is CHRIS oriented, since it takes advantage of the hyperspectral and multiangular capabilities of CHRIS, and also can include the platform temperature information to improve the results. However, the general nature of the procedure allows it to be applied to any push-broom imaging spectrometer.

In addition to the VS noise produced in the image formation process, the transmission of CHRIS channel 2 (odd and even pixels from each CCD row are read in parallel) randomly fails, producing anomalous values called dropouts at the odd pixels in some image rows. Dropouts hamper the operational use of CHRIS images, since latter processing stages are drastically affected by these anomalous pixels [20]. These errors must be corrected by using both spatial and spectral information of the anomalous pixel and its neighbors.

In this work, we focus on modeling and correcting the coherent spatial and spectral noise patterns produced by these systematic yet hardly predictable disturbances. We describe in detail the dropout and VS-correction algorithms, which are currently being implemented in the BEAM Toolbox [21,22] software for

the preprocessing of CHRIS/PROBA data. The rest of this paper is outlined as follows. In Section 2, we focus on presenting, modeling, and correcting the coherent spatial and spectral structures produced by systematic disturbances in the CHRIS instrument. In Section 3, a short description of the employed CHRIS images is given. Results of the methods and the characterization of CHRIS VS are presented in Section 4. Finally, discussion and concluding remarks are given in Section 5.

2. Methodology

A. Definition of Terms

A hyperspectral image consists of two spatial dimensions (along track and across track) and one spectral dimension (wavelength). This hyperspectral image is registered by the instrument in a data cube, where the along-track dimension at the Earth's surface, y , corresponds to the image-line dimension l (distributed in the vertical direction of the image); the surface across-track dimension, x , corresponds to the line-pixels dimension p (distributed in the horizontal direction of the image and CCD); and the spectral dimension, λ , corresponds to the image band b (distributed in the vertical direction of the CCD). These correspondences among the Earth's surface, the instrument CCD, and the hyperspectral data cube are depicted in Fig. 2. The size of the hyperspectral data cube can be written in the form $N_l \times N_p \times N_b$, where N_l is the number of image lines, N_p is the

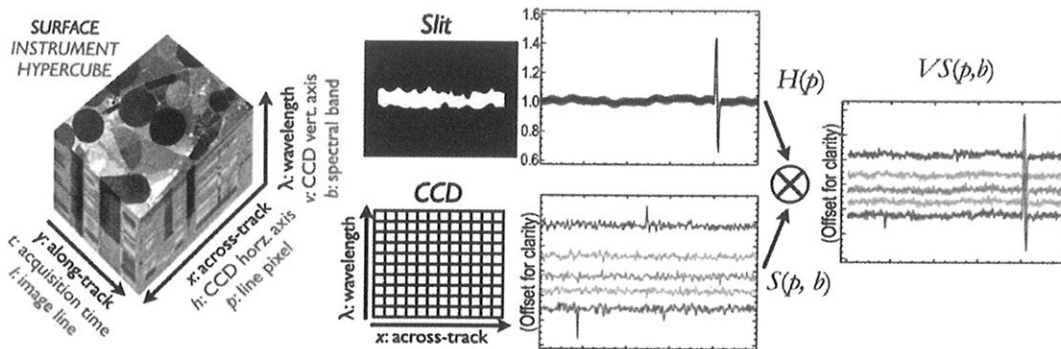


Fig. 2. (Color online) Formation process of the VS, $\nu(p, b)$, from the combination of the nonuniform CCD pixel response, $S(p, b)$, and the slit optical response, $H_x(p)$, which are constant in columns.

number of pixels per line, and N_b is the number of spectral bands. The incoming radiance is integrated over the spatial and spectral response of the system for a given detector element (p, b) of the CCD array. The relation between the incoming at-sensor radiance from the Earth's surface, $L(x, y, \lambda)$ ($\text{W m}^{-2} \text{sr}^{-1} \text{nm}^{-1}$), and the value registered by the CCD, $I(l, p, b)$ (a digital number), can be defined as

$$I(l, p, b) = S(p, b) \int_{y \in l} \int_{x \in p} \int_{\lambda \in b} L(y, x, \lambda) H(x, \lambda) dy dx d\lambda + S_0(l, p, b), \quad (1)$$

where $H(x, \lambda)$ represents the optical system response, $S(p, b)$ is the CCD sensitivity, and $S_0(l, p, b)$ contains all the analog offset errors and random noise. In Eq. (1), it is worth noting that the vertical dimension of the image is related to the time when the image line, l , was acquired. In addition, the image values, I , and CCD sensitivity, S , are expressed as a function of the image pixels and bands, (p, b) . Hence, we assume a one-to-one correspondence between the image pixels and bands and the CCD columns and rows, respectively. However, usually a certain number of CCD columns or rows are binned to form the final image (e.g., reducing the spatial or spectral resolution to increase the radiometric accuracy). In this case, some lines and columns of $I(l, p, b)$ would be summed, but all the presented formulation is still valid.

If the instrument works correctly [5], the spatial and the spectral dimensions (orthogonal dimensions of the CCD) are independent, and they can be processed separately. Therefore, the optical system response can be expressed as $H(x, \lambda) = H(x)H(\lambda)$, where $H(x)$ corresponds to the slit response and $H(\lambda)$ corresponds to the instrument chromatic response, which in turns defines the wavelength and bandwidth of each band. Thus, the slit response is constant for all the lines and bands of a given image, and independent from pixel to pixel.

Assuming a smooth optical response, the integral of the incoming radiance over the optical response of the system in Eq. (1), which represents the radiance

at the focal plane array of the CCD, can be approximated as

$$\int_{y \in l} \int_{x \in p} \int_{\lambda \in b} L(y, x, \lambda) H(x) H(\lambda) dy dx d\lambda = L(l, p, b) H_x(p) H_\lambda(b), \quad (2)$$

where $H_x(p)$ and $H_\lambda(b)$ represent the contribution of the spatial and spectral response to the calibration coefficient of the detector element (p, b) . Then, the relation between the incoming radiance and the value registered by the CCD, Eq. (1), can be written as

$$I(l, p, b) = L(l, p, b) H_x(p) H_\lambda(b) S(p, b) + S_0(l, p, b). \quad (3)$$

Most existing CCD sensors allow an accurate correction of dark current offsets, thus making $S_0(l, p, b)$ negligible, i.e., with only random noise of zero mean and low amplitude remaining. In addition, the provided CHRIS images are radiometrically corrected (so the units of I are radiance units instead of digital numbers). CHRIS products [23] are processed by using an improved radiometric calibration; the calibration was poor in previous versions (with underestimation by up to a factor of 2 of the sensor measurements in the near IR). In [12,24], the authors showed that CHRIS images present an accurate spectral radiometric calibration that allows us to remove the dependency on the spectral response $H_\lambda(b)$. Hence, assuming that $S_0(l, p, b) \simeq 0$ and $H_\lambda(b) \simeq 1$, Eq. (3) is reduced to

$$I(l, p, b) = L(l, p, b) H(p) S(p, b) = L(l, p, b) \nu(p, b), \quad (4)$$

where the VS produced by the combination of the two nonuniform spatial responses is denoted $\nu(p, b)$. A spectral band b will be acquired by the same row of CCD elements, and each image column p will be affected by a different CCD pixel response $S(p, b)$ and a different optical slit response $H(p)$ (equal for

all spectral bands). Therefore, the resulting multiplicative noise $\nu(p, b)$ is constant in image columns and superimposes a systematic pattern of noise organized by vertical lines. The formation of the stripe noise is depicted in Fig. 2.

The physical interpretation of satellite data needs an accurate sensor characterization that corrects the provided (radiometrically calibrated) product, $I(l, p, b)$, to yield values as close as possible to the desired at-sensor radiance, $L(l, p, b)$. Therefore, the procedure consists in finding the set of correction coefficients, which characterize the VS $\nu(p, b)$, to retrieve the true radiance $L(l, p, b) = I(l, p, b)/\nu(p, b)$.

B. Dropout Correction

The process of estimating and correcting VS patterns directly from the image is drastically affected by dropout errors, since these pixels present anomalous values (usually negative) in some bands. Therefore, before VS correction can be carried out, dropout errors must be corrected in order to use all the lines of the image. For this reason, CHRIS products [25] include a quality mask that indicates pixel saturation and occurrence of errors: useful pixel, dropout pixel, and saturated pixel. The problem is that this mask sometimes fails to mark dropout pixels and, in addition, older versions of CHRIS products do not include the mask at all.

1. Dropout Detection

To perform the dropout detection we have to create a mask of the same size as the image and find rows with dropouts. The problem with the nonmasked pixels is that they do not present negative values (their values are of the order of magnitude of the signal) but they always occur in odd columns. Therefore, whether the mask with the dropouts is available or not, we need to improve or create the mask, adding undetected dropouts.

The anomalous pixels (dropouts) are found as follows:

1. We assume that the difference between contiguous pixels in a row is small. The difference between a correct pixel and its neighbor should be equal to or smaller than the difference with the pixel two columns away, except when the neighbor is a dropout. This assumption should be true for all the odd pixels of the row.

- For odd pixels, which may be dropouts, the square difference from neighboring even pixels that are certainly correct,

$$D_{\text{all}}(l, b) = [I(l, p, b) - I(l, p + 1, b)]^2, \\ p = 1, 2, \dots, N_p - 1, \quad (5)$$

should yield high differences in the presence of dropouts.

- For even pixels, which are certainly correct, the square difference from the following even pixel,

$$D_{\text{even}}(l, b) = [I(l, p, b) - I(l, p + 2, b)]^2, p \\ = 2, 4, \dots, N_p - 2, \quad (6)$$

should yield low differences in all cases (depending on the surface changes in the across-track direction).

2. The surface and VS affect differences between contiguous columns; thus the median is used to obtain a robust estimator of the average difference between pixels for the whole line.

3. Finally, all odd pixels of the line are labeled as dropout noise if the difference between neighbors is 50% higher than between even pixels, i.e., $\text{median}(D_{\text{all}}(l, b))/\text{median}(D_{\text{even}}(l, b)) > 1.5$.

2. Dropout Restoration

Once the dropout errors have been detected, they must be corrected by the use of both spatial and spectral information of the anomalous pixel and its neighbors. Each invalid pixel value is replaced by a weighted average of the values of the neighboring pixels. To avoid the poor performance of spatial filters (local average) in border or inhomogeneous areas [16,26], the contribution of each pixel (i, j) of a given neighborhood (C) of size 3×3 is weighted by its similarity to the corrected pixel, $I(l, p, b)$. In particular, this similarity weight is the inverse of the Euclidean distance between the spectral signature of the pixels, which is calculated locally by using the n_b upper and bottom spectral bands closer to the corrected band b :

$$W(i, j) = \left\{ \sum_k [I(l, p, b) - I(l + i, p + j, b + k)]^2 \right\}^{-1/2}, \\ k = -n_b, \dots, -1, 1, \dots, n_b. \quad (7)$$

The final weight matrix, W_C , is modified to have zero values for the pixels not belonging to the given neighborhood C , and it is normalized to sum to one, i.e., $W_C(i, j) = C(i, j)W(i, j)/\sum_{i, j} C(i, j)W(i, j)$. Finally, the new value of the dropout is calculated as

$$I(l, p, b) = \sum_{i, j} I(l + i, p + j, b)W_C(i, j), i, j = -1, 0, 1. \quad (8)$$

The result of this process is similar to a spatial interpolation but taking into account the similarity with neighbors. It is worth noting that the values of bands with errors (indicated by the CHRIS quality mask) are not considered during this process.

The correction of the dropout errors can be carried out independently of the VS correction. However, the VS noise introduces different multiplicative factors in image columns that can affect the new pixel value if the local average is performed by using contiguous columns. Therefore, if one performs the dropout

correction before the VS correction, only the values of the vertical neighbors (C_2) must be used to avoid the effect of VS. After VS removal, it is possible to perform a second correction based on the four-connected (C_4) or eight-connected (C_8) neighbors:

$$C_2 = \begin{pmatrix} 0 & 1 & 0 \\ 0 & 0 & 0 \\ 0 & 1 & 0 \end{pmatrix}, \quad C_4 = \begin{pmatrix} 0 & 1 & 0 \\ 1 & 0 & 1 \\ 0 & 1 & 0 \end{pmatrix},$$

$$C_8 = \begin{pmatrix} 1 & 1 & 1 \\ 1 & 0 & 1 \\ 1 & 1 & 1 \end{pmatrix}. \quad (9)$$

C. Vertical Striping Correction

The objective of VS correction methods is to estimate the correction factor, $\nu(p, b) = H(p)S(p, b)$, of each spectral band to correct all the lines of this band. The main assumption consists in considering that both slit (H) and CCD (S) contributions change from one pixel to another (high spatial frequency) in the across-track direction (p) but are constant in the along-track direction (l), i.e., during image formation, while the surface contribution (L) presents smoother profiles (lower spatial frequencies) in the across-track dimension.

1. Vertical Striping Correction Methods

In the literature, all the VS reduction approaches applied to CHRIS take advantage of the constant noise factors in the image columns [3,16–19]. Basically, each image's column is averaged, resulting in an averaged line (along-track), and then the noise profile is estimated in the across-track direction for each band. By averaging image lines (using an integrated line profile) the surface contribution is smoothed, the additive random noise is cancelled, and the VS pro-

file remains constant. Consequently, the surface contribution presents lower spatial frequencies in the integrated line profile and can be easily separated from the VS (high frequencies) by applying a filter with a suited cutoff frequency.

Figure 3(a) shows the three steps of the method proposed in [3]:

A. Each band is averaged in lines (along-track direction), yielding one integrated line profile per band: $\alpha(p, b) = \int_1^{N_l} I(l, p, b) dl = \nu(p, b) \int_1^{N_l} L(l, p, b) dl = \nu(p, b)\beta(p, b)$.

B. A low-pass filter (LPF) is applied by using a moving-window algorithm that flattens the profile $\alpha(p, b)$ by convolving it with a Gaussian weighting function w : $\beta(p, b) = \text{LPF}\{\alpha(p, b)\} = \int w(p-k)\alpha(p, b) dk$. In this kind of filter, the cutoff frequency f_c defines the standard deviation of the Gaussian window, $\sigma \sim 1/f_c$.

C. Since $\hat{\beta}(p, b)$ contains mainly the surface contribution, the shape of the VS factors can be obtained by the ratio $\hat{\nu}(p, b) = \alpha(p, b)/\hat{\beta}(p, b)$. Thus, the corrected image is calculated as $\hat{L}(l, p, b) = I(l, p, b)/\hat{\nu}(p, b)$.

Figure 3(b) shows the method implemented in [17] to correct CHRIS images. The main difference from the previous method is the use of logarithms to transform the multiplicative noise into additive noise in order to improve the filtering as follows:

A. Each band is averaged in lines, yielding one integrated line profile per band, $\alpha(p, b)$.

B. The averaged profile is log transformed: $\log_\alpha(p, b) \equiv \log(\alpha(p, b)) = \log(\nu(p, b)) + \log(\beta(p, b))$.

C. A LPF is applied to eliminate high-frequency variations (coming from the noise ν) and to estimate the surface contribution: $\log_\beta(p, b) = \text{LPF}\{\log_\alpha(p, b)\}$.

D. High-frequency variations (considered the noise) are obtained: $\log_\nu(p, b) = \log_\alpha(p, b) - \log_\beta(p, b)$.

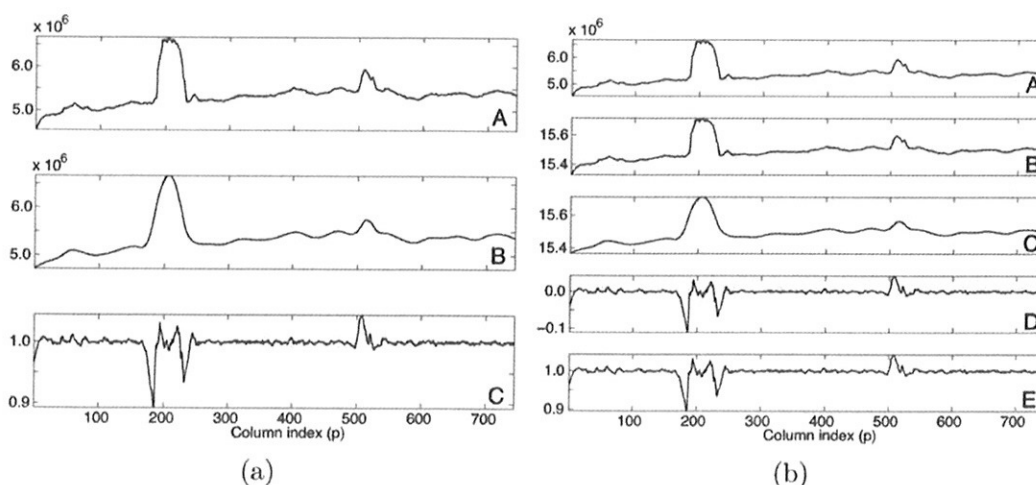


Fig. 3. Example of the processing steps of two different VS reduction methods proposed in (a) [3] and (b) [17] (profiles of the last band of CHRIS_EI_060130_63A1_41 image taken over Heron Island).

E. The VS factors are obtained by calculating the inverse of the logarithm: $\hat{\nu}(p, b) = \exp(\log_{\nu}(p, b))$.

Theoretically, when the line profile is being filtered the first approach should give poor results because it is affected by multiplicative noise, and this is equivalent to a convolution in the frequency domain. This is the main reason to propose the second approach, but, in practice, both approaches give equivalent results. This outcome can be explained, because features of the multiplicative noise present a mean close to one ($f = 0$ and $A = 1$) and high-frequency components of low amplitude ($\uparrow f$ and $A \approx 0.1$). Therefore, when performing the convolution of the signal and noise in the frequency domain, the power spectral density of the signal at low frequencies is not affected. Since both methods provide equivalent results, we consider them a single method, and hereafter we refer to them as the standard method.

The standard method can fail for several reasons, such as high-amplitude changes in the VS, which affect the performance of the LPF (wrong estimation of the surface contribution), producing an overestimation or underestimation in the correction factors of the neighboring columns. In [16], an iterative method that corrects the effect of these high striping values is presented. However, as proposed in the next subsection, these effects can be also avoided by using more advanced filtering techniques that use a weighting function.

2. Robust Vertical-Striping-Correction Method

One of the main drawbacks of the methods proposed in the literature is that they do not explicitly take into account the possible high-frequency components of the surface. In images presenting structures or patterns in the vertical direction, the averaged profile $\alpha(p, b)$ may present high-frequency contributions that are due to the surface. This will be interpreted as VS when $\nu(p, b)$ is estimated (see the selected example in Fig. 3), and some columns will be corrected with wrong values, worsening the final image.

The proposed correction method is also based on the hypothesis that the vertical disturbance presents higher spatial frequencies than the surface radiance. However, it models the noise pattern by suppressing the surface contribution in the across-track direction in two different ways: first, by avoiding the high-frequency changes due to surface edges and, second, by subtracting the low-frequency profile.

The surface can present high spatial frequencies due to the surface texture, which has low amplitude changes, or due to changes in the land-cover type, which can produce great changes in amplitude that are a problem in the destriping process. In principle, in one spectral band both the surface and the noise contributions are mixed, and is not possible to distinguish which of them causes the changes in the radiance amplitude between contiguous columns. However, the spectral signature of pixels from cur-

rent hyperspectral sensors can provide helpful information about the land-cover changes. Considering the spectra of two contiguous pixels, p_1 and p_2 , just in the boundary between two land-cover types, three factors affect the spectral change: (i) differences between the true spectra of both surfaces (in shape and magnitude); (ii) the varying CCD sensitivity $S(p, b)$, which modulates the spectral signature as a multiplicative noise of low variance; and (iii) the varying multiplicative factor that is due to the slit $H(p)$, which scales the magnitude of the whole spectral signature. Among these three factors, the first one will produce the greater change, the second one will be a second-order factor when the spectral similarity is compared, and the third one will not affect the final result if the selected spectral distance is invariant to scaling by a positive factor. Therefore, we can apply a filter in the across-track direction of the hyperspectral image to find the surface borders that introduce high frequencies in the across-track profile. The next subsections explain how pixels corresponding to borders are not employed when computing the integrated line profiles.

Spatiospectral Edge Detection. We propose a spatio-spectral filter based on two-dimensional convolution filters, which are commonly used in gray-scale image processing, such as the derivation filter and the Roberts operator [27]. In this work, the horizontal edge pixels of the processed hyperspectral image are found by using the derivative filter in the horizontal direction $K = \begin{pmatrix} 1 & -1 \\ 0 & 0 \end{pmatrix}$. To apply these tech-

niques to hyperspectral images, taking the spectral dimension into account, it is not possible to directly compute the convolution of the kernel matrix and the three-dimensional hypercube. In our proposal, a spectral distance is first computed between the spectrum of the pixel linked to the position with value $K(i, j) = -1$ in the kernel matrix (reference pixel), and the rest of the neighboring pixels (forming a matrix D of distances with the value $D(i, j) = 0$ for the reference pixel). Then, the sum of the product of the elements of the kernel and the distance matrix is computed, $\sum_{i,j} K(i, j)D(i, j)$, and the resulting value is assigned to the reference pixel (i, j) . The main difference between this method and gray-scale image processing is that only one position of K can present the value -1 , which indicates at each moment the pixel that is being used as a reference to compute the spectral distances. Once this process is applied to all the pixels, a sensitivity threshold is defined. All pixels with values higher than the threshold (i.e., pixels whose spectral signatures differ from that of their neighbors) are identified as edges.

Concerning the spectral distance D , the spectral angle distance is used, since it is invariant to multiplicative scaling [28] and will not be affected by the VS of the slit:

$$D(\mathbf{x}_1, \mathbf{x}_2) = \arccos(\langle \mathbf{x}_1, \mathbf{x}_2 \rangle / (\|\mathbf{x}_1\| \|\mathbf{x}_2\|)), \quad (10)$$

where \mathbf{x}_1 and \mathbf{x}_2 are the vectors containing the spectral signature of the pixels whose spectral distance is being calculated, $\langle \cdot, \cdot \rangle$ is the dot product operator, and $\| \cdot \|$ is the quadratic norm. Finally, to find an optimum threshold for each image, but also accounting for a significant number of lines to compute the smoothed integrated line profiles, an iterative empirical procedure is followed. The procedure starts with a threshold equal to zero iteratively increased until 60% of nonedge pixels in the column that presents more edge pixels is ensured, i.e., $\sum_{i,j} K(i,j) D(\mathbf{x}(l,p), \mathbf{x}(l+i,p+j)) > \text{threshold}$.

Vertical Striping Removal. A critical point of the proposed approach is how to remove edge pixels when the integrated line profiles are computed. If all image lines that present at least one edge pixel are removed, it is probable that only a few or even none of the lines can be used in the averaging. On the other hand, if the edge pixels are removed and only the remaining pixels of the line are used for averaging, then the problem is not solved, since the high frequencies are still there (think of a step profile where only one point is removed). The only way to remove the edges is to work in the across-track spatial derivative domain, where the homogeneous areas before and after the edge present values close to zero and the spikes of edge pixels can be substituted, interpolating prior to the integration in the along-track direction. In this simple way, all high-frequency contribution by the surface is removed from the integrated line profile before the low-pass filtering, and then the estimated VS is independent of the surface patterns.

Figure 4 shows the steps of the proposed method:

A. Apply logarithms to transform the multiplicative noise into additive noise [$\log(I(l,p,b))$].

B. Transform the hyperspectral data cube into the across-track spatial derivative domain, which is equivalent to high-pass filtering: $\theta(l,p,b) = \frac{\partial}{\partial p} \log(I(l,p,b)) = \log(I(l,p,b)) - \log(I(l,p-1,b))$, for $p > 1$ (note that the first column derivative is fixed to zero, $\theta(l,1,b) = 0$).

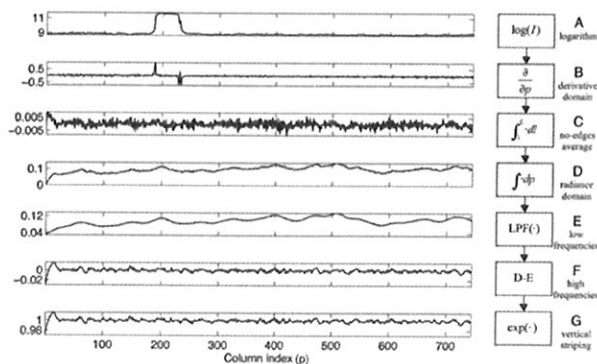


Fig. 4. Example of the processing steps of proposed VS correction method (profiles of the last band of CHRIS_EI_060130_63A1_41 image taken over Heron Island).

C. Average the lines of each band in the along-track direction but avoiding the edge pixels found with the spatio-spectral edge detection: $\xi(p,b) = \int_1^{N_l} \theta(l,p,b) dl$. Working in the derivative domain has allowed our method to avoid edge pixels, and it also elevates the noise level temporarily because the surface power spectrum is concentrated in the low-frequency region, whereas the VS is spread over all of the spatial frequency spectrum [29]. Nevertheless, if the LPF is applied in the derivative domain, the committed errors by the LPF will accumulate throughout the integration in the across-track direction. Therefore, after applying the along-track LPF, data is integrated across-track to retrieve the signal in the radiance domain.

D. Integrate in the across-track direction (cumulative sum in p): $\phi(p,b) = \sum_{i=1}^p \xi(i,b)$, i.e., the integration bias is corrected at the end of the process.

E. Apply a LPF in the across-track direction to eliminate the high-frequency variations coming from the noise ν and estimate the surface contribution: $\varphi(p,b) = \text{LPF}\{\phi(p,b)\}$.

F. Obtain the high-frequency variations (considered to be the noise) by subtracting the low frequencies: $\psi(p,b) = \phi(p,b) - \varphi(p,b)$. The error introduced during the integration process consists in a constant value for each band. Nevertheless, as the VS is corrected independently for each band, the VS in the logarithmic domain should present zero mean (gain close to 1 in the radiance image). Therefore, the offset errors are corrected by subtracting the mean value: $\psi(p,b) = \psi(p,b) - 1/N_p \sum_p \psi(p,b)$.

G. Finally, obtain the VS factors by calculating the inverse of the logarithm $\hat{\nu}(p,b) = \exp(\psi(p,b))$.

Multangular Vertical Striping Removal. Thanks to the sequential acquisition of CHRIS of the same scene from five different angles, we can also improve the robustness of the proposed algorithm by using all of the multiangular images of one acquisition together. As mentioned before, the VS due to the instrument slit is temperature dependent. Although temperatures recorded for different acquisitions have shown differences higher than 8°C, changes within a single acquisition (five multiangular images) are less than 0.5°C. Therefore, images of one acquisition present the same VS pattern while they are recording different spatial patterns from the same Earth area (owing to perspective, platform motion, and Earth rotation). One can take advantage of this fact to improve the estimation of the VS by considering the five images a single longer hyperspectral image, which is formed by stacking the multiangular images in the along-track direction, i.e. a hypercube with the same number of columns N_p and bands N_b but with $5 \times N_l$ lines with a different spatial distribution of similar surface types (similar spectra). When a higher number of lines are processed together, the surface contribution is smoother, and the estimation of the VS is more accurate.

3. Data Material

A. CHRIS Database

CHRIS acquisition modes present different spatial resolution and spectral bands. In addition, they can be differenced in spatially binned (mode 1, with 372 columns) or unbinned (modes 2, 3, 4, and 5 with 744 columns) modes in the across-track direction. As a consequence, the performance of the proposed algorithm has to be tested on a large number of sites of different natures, for several acquisition modes, and covering the full range of possible sensor temperatures. For this study, a data set consisting of 79 acquisitions over 21 of the core sites of the PROBA mission was considered. In particular, it contains 274 mode 1 images from 55 acquisitions of 14 test sites, and 113 mode 2 images from 24 acquisitions of 7 test sites. In these acquisitions, the instrument's temperature ranges from 1°C to 9°C, since the platform temperature changes through the year and within each orbit (CHRIS does not have thermal regulation); the nominal temperature of the detector is 5°C.

B. Synthetic Images

To quantitatively validate the proposed method, not having available any prelaunch CCD–slit characterizations, a set of realistic synthetic images were generated based on three CHRIS acquisitions taken over the site of Barrax (BR, Iberian Peninsula, Spain), Heron Island (EI, Great Barrier Reef, Australia), and Port of Valencia (PC, Mediterranean Coast,

Spain). These images were selected for the study to take into account different CHRIS acquisition modes, surface types, and spatial textures and patterns (soil, vegetation, sea, clouds, urban areas, etc).

The synthetic images were generated free of noise as follows. First, we manually labeled the land-cover classes in a corrected CHRIS image. In multispectral image processing, the assumption that the distribution of image classes can be approximated as a mixture of normally distributed samples is widely accepted. Therefore, we considered each homogeneous land cover as a normal distribution and used the labeled regions of the CHRIS image to estimate the parameters of a Gaussian mixture model (mean and covariance matrix for each class). Once we had the ground truth with the areas covered by the different spectral classes, the parameters of the Gaussian mixture model and the priors, we generated a synthetic image as follows: (i) the required number of samples for each class was randomly generated from the corresponding N_b -dimensional Gaussian distribution; (ii) a proper texture of gray level values was assigned to each region (or class) in the image that simulates the natural variability distribution within the region; and (iii) the generated spectra of each class were shortened depending on their brightness (intensity) and were iteratively assigned to the image location that presented the next higher gray level value in the texture image. Following this procedure, the final image preserved the spatial distribution of the classes, while introducing a realistic variability within each class. Figure 5 shows the

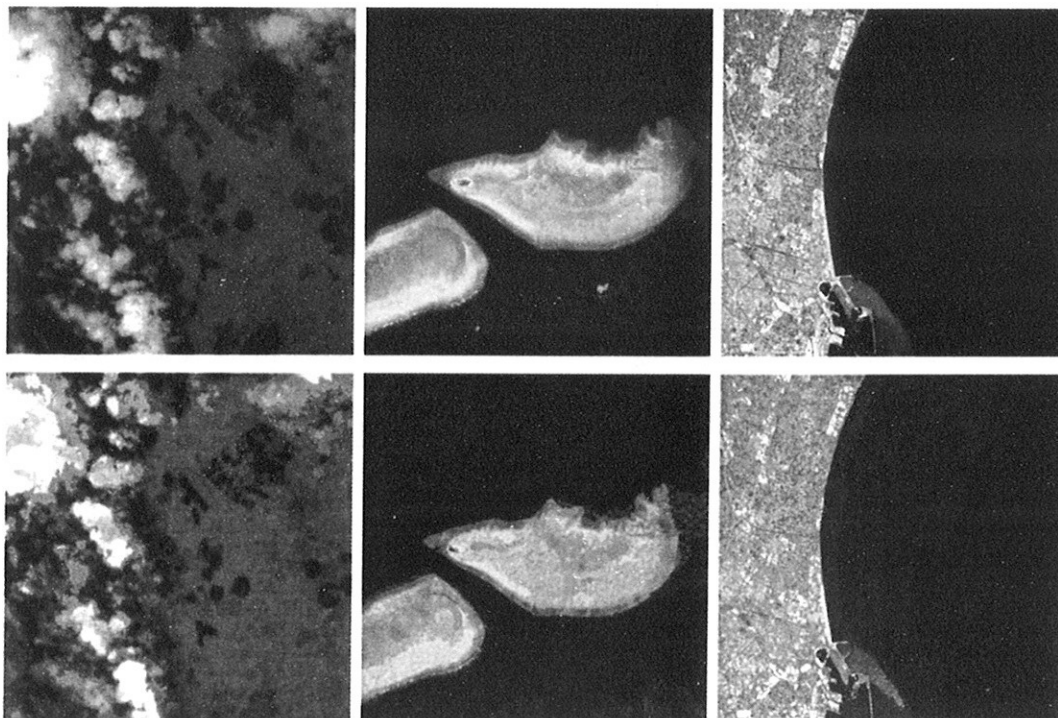


Fig. 5. (Color online) Pictures of the CHRIS original (upper row) and synthetic noise-free (lower row) images over the test sites of BR-2005-07-17 (mode 1), EI-2006-01-30 (mode 2), and PC-2005-05-18 (mode 2).

original corrected real images and the synthetic noise-free images over the test sites (BR-2005-07-17, EI-2006-01-30, and PC-2005-05-18). It is worth noting that the synthetic images preserve the real surface contribution and texture.

Finally, synthetic multiplicative noise coming from the entrance slit and CCD array was incorporated into the generated synthetic noise-free images. First, the effect of the uneven slit width on the light arriving at the CCD was modeled [Fig. 6(a)] by using the superposition of four sinusoids of different characteristics modulating the unity gain (one high-frequency component, two mid-frequency components, and one low-frequency component with amplitudes between 0.01 and 0.03). Two more sinusoids of large amplitude (0.4 and 0.2) but limited extension (only one cycle length in about 5 pixels width, and a half-cycle, respectively) were placed at two given positions to simulate the effect of particularly strong stripes (in the CHRIS case due to dust particles stuck onto the slit). Second, the simulated CCD consists of two mixed distributions: a normal distribution of unity mean and 0.005 variance, which would represent a fair response of a regular CCD, and a Gamma distribution of order 3 for a few elements of the CCD, which accounts for anomalous or defective pixels (leakers) with reductions in gain between 6% and 13%. Figure 6(b) illustrates the synthetic multiplicative noise with the combined contribution of the slit and the CCD. The simulated noise ranges from 0.7 to 1.3 (slightly lower values have been reported for CHRIS in [4,16]). This rather simple approach of synthetically generating noise for the simulated scenes allows the limitations of the algorithm to be easily determined by testing which frequencies are properly removed by the noise-removal algorithms and those pass through undetected.

4. Experimental Results

A. Method Performance

One of the main differences between the methods presented in Section 2.C.1 and the proposed method comes from the employed LPF. In the case of CHRIS images, in which some columns are affected by high noise factors due to slit nonuniformities, it is critical to employ a filter robust to outliers. To perform a fair

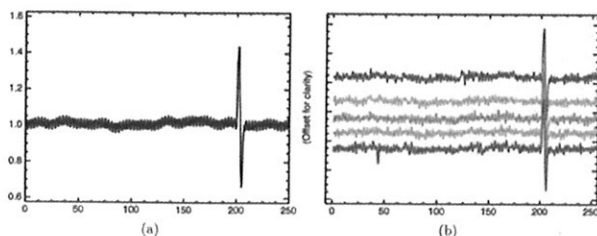


Fig. 6. (Color online) Synthetic multiplicative noise (first 250 image columns shown for proper visualization). (a) Noise profile coming from the entrance slit (slit VS). (b) Noise profile applied to each spectral band that is obtained multiplying the slit VS by the CCD response for each band in the across-track direction.

comparison between methods, the same LPF is used in both cases. The smoothing is based on a robust regression algorithm that assigns lower weight values to outliers. The filter bandwidth is adjusted for each band to pass low-frequency components at up to 99% of the cumulative power spectral density of the along-track integrated profile of each band. The assumption of having noise below about 1% of the total energy is a reasonable value from the data acquired prior to launch [17].

1. Results for Synthetic Images

The first battery of experiments is concerned with assessing the estimation of the VS factors, and thus the accuracy of the noise reduction. For this purpose, the three synthetic hyperspectral images with a known simulated noise pattern are used. By knowing the true noise factors, it is possible to quantify the noise reduction in the corrected images. Although it is possible to obtain and compare the signal-to-noise ratio of the synthetic noisy images and the corrected ones, the VS is not actually a random noise. Therefore, Table 1 shows the difference between the actual and the estimated VS factors ($\nu(p, b)$ and $\hat{\nu}(p, b)$) for both methods in terms of the mean error (ME), mean absolute error (MAE), and root mean-squared error (RMSE). Results show that the proposed method produces better estimations of the VS factors for all the images. The bias in the estimated VS, which yields negative ME for all the images and methods, is due to the low frequencies present in the simulated VS that cannot be removed by any method [see Fig. 7(a)]. The obtained MAE values (about 0.013) indicate that both algorithms provide good image correction, since the multiplicative noise applied to the synthetic images $\nu(p, b)$ ranges from 0.7 to 1.3. When the regression and the residuals of Fig. 7(b) are analyzed, one can also appreciate that both high and low values of VS are underestimated or overestimated, respectively, because of the low-pass filtering.

To better quantify the global performance of the proposed method, Table 1 also shows the relative improvement of RMSE when our method is used ($\sim 3\%$). That is, results from both methods seem to be very similar. In fact, in a one-way analysis of variance performed to compare the means of the residuals [30], no significant statistical differences were observed between both methods. This result can be explained in that our method intends to be more robust to surface changes; it will solve critical problems in some image columns, but in the rest of them both methods follow a similar procedure.

2. Results for Real Images

The second battery of experiments is concerned with assessing the noise reduction in real images. In this case, neither the true values of the VS factors nor the noise-free images are available to quantify the noise reduction in a single image. However, robustness of the algorithms to changes in the surface can be

Table 1. Mean error (ME), mean absolute error (MAE), and root mean-squared error (RMSE) for actual and estimated VS correction factors for synthetic images

Image Method	BR-2005-07-17		EI-2006-01-30		PC-2005-05-18	
	Standard	Proposed	Standard	Proposed	Standard	Proposed
ME $\times 10^{-2}$	-0.471	-0.429	-0.452	-0.398	-0.486	-0.413
MAE $\times 10^{-1}$	0.131	0.127	0.126	0.120	0.149	0.145
RMSE $\times 10^{-3}$	0.104	0.101	0.132	0.126	0.198	0.192
Δ RMSE [%] ^a		2.48		4.00		3.09

^aComputed relative improvement of RMSE obtained when using the proposed method.

compared by using the full database of real images. For this purpose, we take into consideration two CHRIS acquisition circumstances: (i) the VS estimated for the five angular images of one acquisition should be equal, but (ii) surface spatial patterns observed from the five viewing angles are different. As a consequence, small variations between the estimated noise profiles for each angle within a multiangular acquisition indicate that the surface is not affecting the algorithm's performance.

Figure 8 shows the scatter plot, for the standard and the proposed methods, of estimated noise variance within each acquisition set. These values are computed as the standard deviation of \hat{v} among the estimations for the five angular images and are averaged for all of the spectral bands and columns. Each point corresponds to a single multiangular acquisition, which consists of up to five images when they are available. Figure 8 shows results for 55 mode 1 acquisitions and 24 mode 2 acquisitions comprising 274 and 113 images, respectively. The scatter plot shows that, in almost all cases, the variation of the estimated noise pattern within one acquisition set is lower for the proposed approach (especially in mode 2 acquisitions), which demonstrates the robustness to surface contribution. Figure 9 shows three illustrative examples of real images of both CHRIS mode 1 (land mode) and mode 2 (water mode). The same area is displayed for the original CHRIS product (left-hand column), the image corrected with the algorithm implemented in [17] (center column), and the image processed with

the noise reduction proposed in this work (right-hand column). Images have been equalized for proper visualization. The first image acquired over Lanier (first row) has been selected to illustrate the standard situation where a noisy image with similar land cover types (bare soils and crops) is properly corrected by both methods. Note that, when the center of the corrected images is enlarged, a residual low-amplitude VS can be observed in the image corrected by the standard approach (Fig. 9, center). The other two images, acquired over Reynold's Creek (second row) and Rame Head (third row), have been selected to better analyze the results shown in Fig. 8, where the proposed method consistently outperforms the standard one. For this purpose, we selected two images for which the proposed algorithm performs especially better than the standard algorithm. Analyzing the characteristics of these two images, one can conclude that both images present a typical situation with high contrast between dark and bright surfaces, such as sea-land and ice-clouds, respectively. In this situation, standard destriping algorithms are affected by the surface contribution, which produces misleading correction factors, producing undesired vertical patterns (even worse than the original noise) at the affected image columns (Fig. 9, center). However, when using the proposed algorithm (Fig. 9, right), noise is clearly reduced

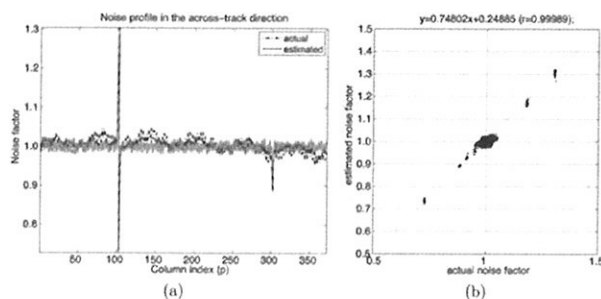


Fig. 7. (Color online) Performance of the proposed method in the estimation of the VS of image BR-2005-07-17 (mode 1): (a) actual and estimated VS; (b) actual versus estimated correction factors.

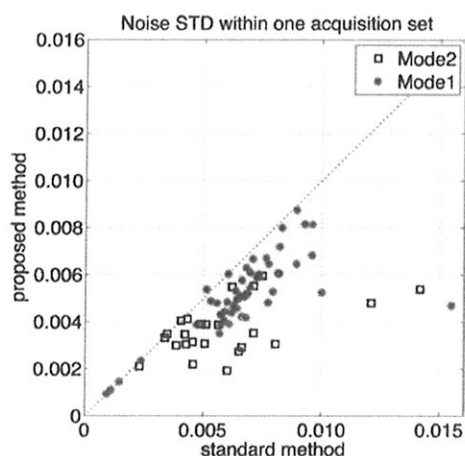


Fig. 8. (Color online) Scatterplot of the standard deviation of the estimated VS factors (computed for each acquisition within the five angles) for both methods.

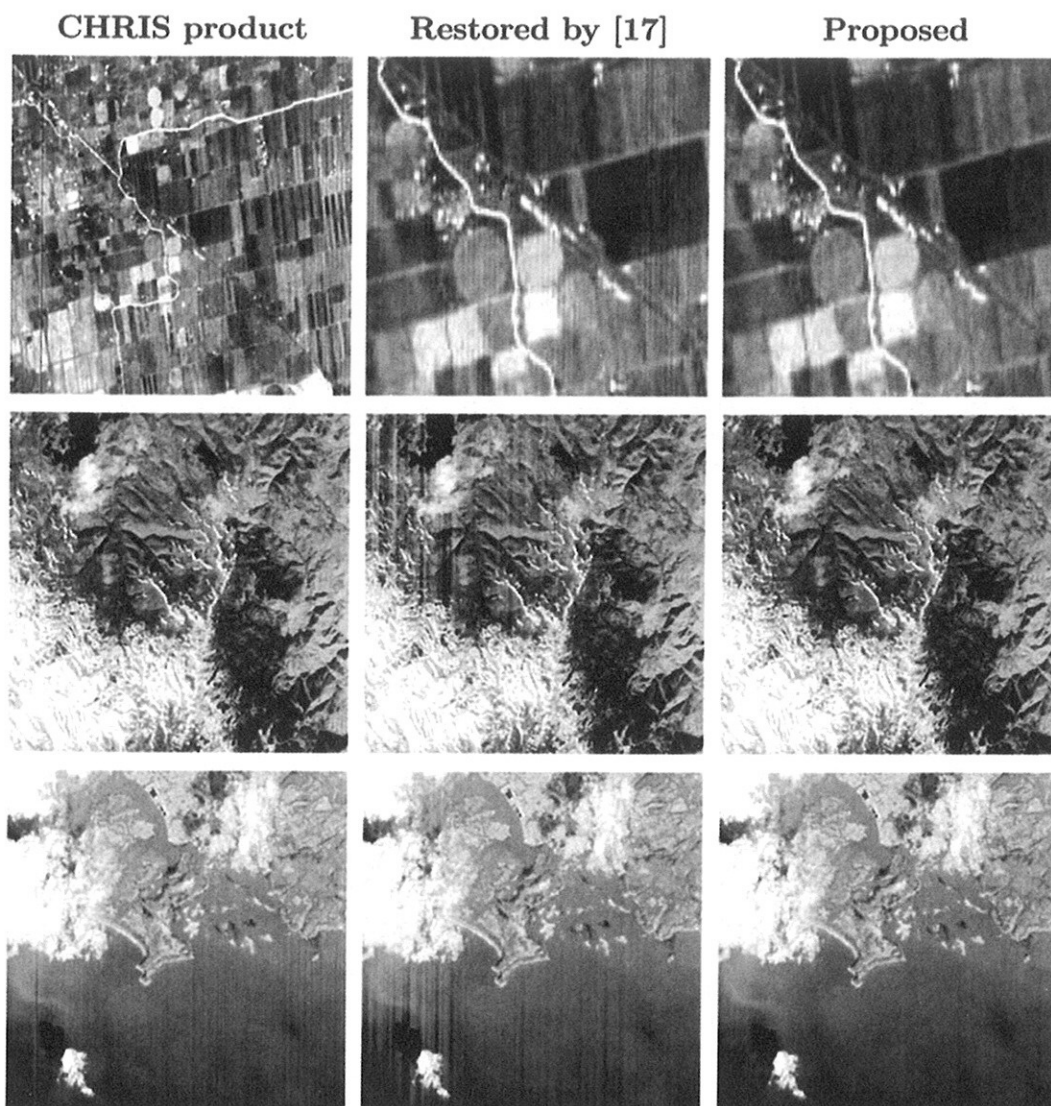


Fig. 9. (Color online) Example of the noise reduction results on real CHRIS images over the test sites of Lanier (Canada, LR-2005-02-22, mode 1), Reynold's Creek (USA, RC-2004-04-23, mode 1), and Rame Head (UK, RH-2003-03-06, mode 2): original CHRIS product (left column), the image corrected with the algorithm implemented in [17] (center column), and the image processed with the proposed algorithm (right column).

even under the presence of anomalous surface transitions, and only some residual low-frequency, low-amplitude pattern can be seen in the dark sea areas. This also explains why, in Fig. 8, the proposed algorithm outperforms the standard algorithm particularly in mode 2 acquisition sets, since mode 2 is the water mode (with higher sensitivity setting), and thus it is probable to find dark water bodies adjacent to bright surfaces.

B. Vertical Striping Characterization and Correction of the Slit Effect

Finally, a result of great value is the characterization of the VS and its dependence on temperature. For this purpose, we corrected a significant number of CHRIS images of the database, obtaining an esti-

mation of the VS pattern, $\hat{v}(p, b) = H(p)S(p, b)$, per image. The sensitivity of the CCD array, $S(p, b)$, is assumed to be characterized by a Gaussian distribution with unit mean. However, applying the logarithmic transformation to the estimated VS changes the multiplicative nature of both terms to additive, $\log(\hat{v}(p, b)) = \log(H(p)) + \log(S(p, b))$, where the term $\log(S(p, b))$ can be safely considered additive noise with zero mean distribution. As a consequence, the VS profile due to the slit, which is constant in columns, can be obtained by averaging in the spectral direction of the CCD and then reverting the logarithm: $H(p) = \exp(\int_1^{N_b} \log(\hat{v}(p, b)) db)$. Moreover, the slit VS profiles of the five angular images can be averaged to obtain only one $H(p)$ per acquisition,

which will be associated with the platform temperature for this given acquisition: $H(p, T)$. Changes in temperature produce a dilation of the slit, changing its width and moving the image of the slit across the detector. These two effects produce a scaling of the slit VS factors and a shift of its shape in the across-track direction, respectively, thus producing a temperature-dependent VS. Figure 10, on the left-hand side, shows a peak of the obtained $H(p)$ profiles for all the analyzed mode 2 acquisitions (mode 2 is shown because it is not binned and presents higher across-track resolution than mode 1). The asterisks represent the actual $H(p)$ values for each pixel column p , and the solid curves are the corresponding spline interpolations in the across-track direction x , which provide a continuous subpixel resolution model of the striping $H(x)$ for each measured temperature T : $H(x, T)$. The curves clearly show the shift and scaling of the VS amplitude with temperature. Taking as reference the VS at $T_0 = 5.5^\circ\text{C}$, we compute the shift in the across-track looking for the lag, $\Delta_x(T)$, of the maximum of the cross-correlation sequence between the analyzed VS, $H(x, T)$, and the reference one, $H(x, T_0)$. Once the shift is corrected, the scaling factor $G_H(T)$ is computed as the slope of the linear regression that better fits $H(x, T)$ to $H(x, T_0)$ in a least-squares sense. In the central and right-hand plots of Fig. 10 we represent the shift $\Delta_x(T)$ and scale $G_H(T)$ of the slit VS as a function of temperature, respectively. It is worth noting that the excellent agreement among the noise profiles estimated from all the real images [Fig. 10(a)] allows us to obtain an empirical model of the slit VS and indirectly confirms the robustness of the algorithm and the consistency of the results.

The estimated $\Delta_x(T)$ and $G_H(T)$ values are used to compensate for the shift and scale of the slit VS $H(x, T)$ and obtain the corresponding slit VS for each acquisition of the database, but expressed at the reference temperature T_0 . The average of all these curves provides us a model of the real slit VS at the reference temperature, denoted $\mathcal{H}(x)$, minimizing the estimation errors. The modeled slit VS for a given temperature T can be recovered from $\mathcal{H}(x)$ as

$$H(x, T) = G_H(T)\mathcal{H}(x - \Delta_x(T)), \quad (11)$$

where $\Delta_x(T_0) = 0$ and $G_H(T_0) = 1$. The value for a given pixel column p is obtained by integrating the width of the pixel photosensible area:

$$H(p, T) = \int_{p-1/2}^{p+1/2} H(x, T) dx. \quad (12)$$

It is worth noting that mode 1 performs a binning of columns in pairs. Therefore, for mode 1 images, we have to simulate the binning in order to obtain the slit VS factors for each image column:

$$H_1(p_{\text{binned}}) = \frac{1}{2}[H_2(p-1) + H_2(p)], \quad (13)$$

where $p = \{2, 4, 6, \dots, 744\}$ and p_{binned} is the pixel number in mode 1 images (372 columns).

Figure 11 shows a segment of the slit VS curves modeled independently from mode 1 and mode 2 acquisitions $\mathcal{H}_1(x)$ and $\mathcal{H}_2(x)$ [Fig. 11(a)] and the scatter plot of mode 1 versus mode 2 [Fig. 11(b)]. Agreement between both results is excellent, except in the highest and lowest anomalous values (VS peaks), where probably the interpolation used to obtain $H(x)$ produces underestimated VS peaks, with this effect being more noticeable in the binned mode 1.

C. Summary of the Complete Processing Chain

In the previous sections, several processing steps have been presented to detect and correct specific noise patterns affecting push-broom hyperspectral sensors. The optimal sequence of algorithms to be applied in order to correct a given image is listed.

1. Dropouts are detected and corrected with the methodology proposed in Subsection 2.B.
2. A rough correction of the VS due to the entrance slit is performed. For a given CHRIS image, the estimation of the slit VS $H(p, T)$ is obtained from the characterization of the VS pattern $\mathcal{H}(x)$ stored in a lookup table. This is done by using Eq. (11) to

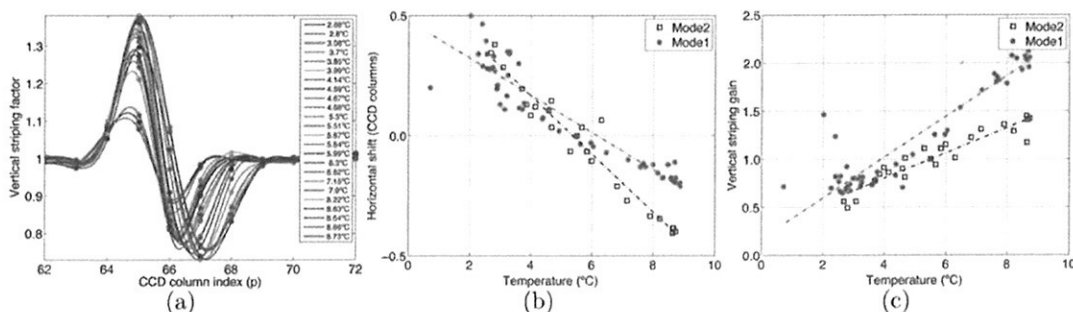


Fig. 10. (Color online) Dependence of CHRIS slit VS on temperature. From left to right: (a) detail of the slit-VS profiles for all the mode 2 acquisitions of the database ($H(p, T)$ and $H(x, T)$); (b) across-track shift of the slit-VS shape as a function of temperature ($\Delta_x(T)$); (c) scaling of the slit VS factors as a function of temperature ($G_H(T)$).

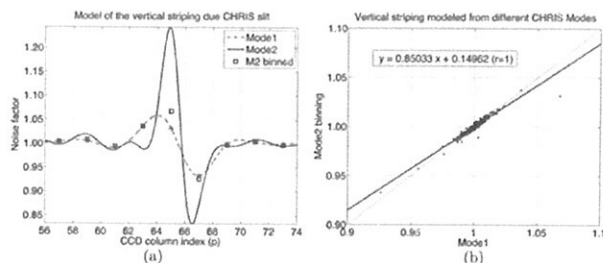


Fig. 11. (Color online) (a) Detail of the real slit VS \mathcal{H} modeled from mode 1 and mode 2 CHRIS images, and the binning of mode 2 closely matching the mode 1 curve. (b) Scatterplot of the modeled mode 1 and mode 2 real slit VS.

include the dependence on the platform temperature T at the given CHRIS acquisition, and then Eq. (12) when the acquisition mode is binned. In Eq. (11), we assume for both the columns' shift and the gain factor a linear dependence on the instrument's temperature: $\Delta_x(T) = -0.12T + 0.65$ and $G_H(T) = 0.13T + 0.28$, respectively, where the coefficients of the linear regression are obtained directly from unbinned data (mode 2) presented in Fig. 10.

3. After the preliminary correction of the VS due to the entrance slit, the robust VS correction method proposed in Subsection 2.C.2 is used to estimate directly from the image (or multiangular image set) the remaining VS for each band $\hat{v}(p, b)$.

4. Finally, obtained factors are used to correct the image column values.

5. Summary and Conclusions

In this paper, we have presented a new technique that faces the problem of removing the coherent noise, known as dropout and VS, usually found in hyperspectral images acquired by push-broom sensors such as CHRIS. First, pixels presenting dropouts are detected and corrected by use of both spatial and spectral information of the dropout pixel and its neighbors. Although it is a cosmetic correction, it is needed, since later processing stages are drastically affected by these anomalous pixel values. Then, the VS pattern is reduced by using an algorithm robust to surface changes. Several algorithms already exist to reduce VS, but most of them assume that the imaged surface does not contain structures with spatial frequencies of the same order as noise, which is not always the case. The proposed method introduces a way to exclude the contribution of the spatial high frequencies of the surface from the process of noise removal that is based on the information contained in the spectral domain. In addition, an element common to most destriping techniques is the application of a LPF, which requires setting a cutoff frequency. Generally this frequency is set to a fixed value, which might not always be the optimal. In our approach, the most adequate cutoff frequency is estimated for each image, and a filter robust to outliers is used.

Synthetic realistic scenes have been created, adding modeled noise, for validation of the method. From

the experiments, we can conclude that the proposed method offers better performance than the standard method, showing a 3% RMSE improvement. Attending to visual inspection on real data, noise is clearly reduced, even under the presence of outliers. Hence, the proposed algorithm, although computationally more expensive, provides more robust performance in different types of scenes, and it is especially recommended for those scenes with sharp transitions between contrasted surfaces. This produces a higher stability of the estimated noise from images within an acquisition set, which has been quantitatively shown for 55 and 24 acquisitions of modes 1 and 2, respectively. These characteristics have permitted us to successfully model the shape of the slit with subpixel resolution and to find a relationship between the sensor temperature and the magnitude and distribution of the VS.

The proposed approach has proved to be robust, stable in VS removal, and a tool for noise modeling. Finally, the general nature of the procedure allows it to be applied for destriping images from other spectral sensors. Currently, the presented method is being implemented in ESA BEAM software as a part of a toolbox for the preprocessing of CHRIS/PROBA data.

This work has been partly supported by the Spanish Ministry of Education and Science under projects DATASAT/ESP2005-07724-C05-03 and CONSOLIDER/CS2007-00018. The implementation of the algorithm has been done in the frame of ESRIN Contract No. 20442/07/ILG (Development of CHRIS/PROBA Modules for the BEAM Toolbox project). The authors also thank ESA and SIRA Technology Ltd. for the availability of the image database, Mike Cutter and Lisa Johns for the assistance provided, and the two reviewers for their valuable comments.

References and Notes

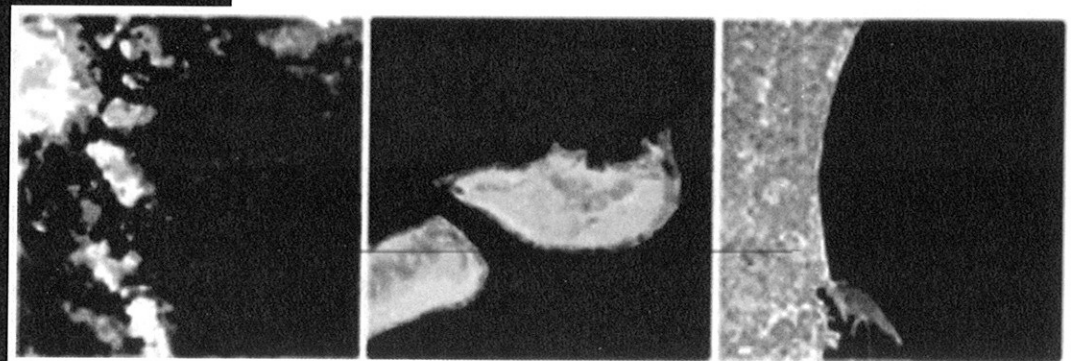
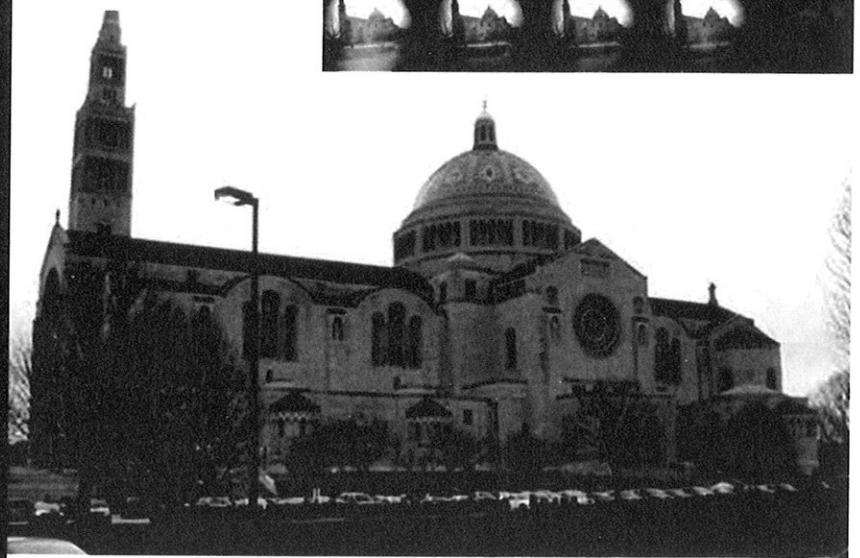
1. B. Aiazzi, L. Alparone, A. Barducci, S. Baronti, and I. Pippi, "Estimating noise and information for multispectral imagery," *Opt. Eng.* **41**, 656–668 (2002).
2. M. Wettle, V. E. Brando, and A. G. Dekker, "A methodology for retrieval of environmental noise equivalent spectra applied to four Hyperion scenes of the same tropical coral reef," *Remote Sens. Environ.* **93**, 188–197 (2004).
3. A. Barducci and I. Pippi, "Analysis and rejection of systematic disturbances in hyperspectral remotely sensed images of the Earth," *Appl. Opt.* **40**, 1464–1477 (2001).
4. A. Barducci, D. Guzzi, P. Marcoionni, and I. Pippi, "CHRIS-PROBA performance evaluation: signal-to-noise ratio, instrument efficiency and data quality from acquisitions over San Rossore (Italy) test site," in "Proceedings of Third CHRIS/Proba Workshop," ESA-SP-593 (European Space Agency, 2005), paper 09_bardu.pdf.
5. P. Mouroulis, R. O. Green, and T. G. Chrien, "Design of pushbroom imaging spectrometers for optimum recovery of spectroscopic and spatial information," *Appl. Opt.* **39**, 2210–2220 (2000).

6. L. Guanter, R. Richter, and J. Moreno, "Spectral calibration of hyperspectral imagery using atmospheric absorption features," *Appl. Opt.* **45**, 2360–2370 (2006).
7. M. Barnsley, J. Settle, M. Cutter, D. Lobb, and F. Teston, "The PROBA/CHRIS mission: a low-cost smallsat for hyperspectral, multi-angle, observations of the Earth surface and atmosphere," *IEEE Trans. Geosci. Remote Sensing* **42**, 1512–1520 (2004).
8. D. Bernaerts, F. Teston, and J. Bermyn, "PROBA (Project for Onboard Autonomy)," presented at the 5th International Symposium on Systems and Services for Small Satellites (La Baule, France, 2000).
9. M. Cutter and L. Johns, "CHRIS data products—latest issue," in "*Proceedings of Third CHRIS/Proba Workshop*," ESA-SP-593 (European Space Agency, 2005), paper 05_cutter.pdf.
10. L. Gómez-Chova, L. Alonso, L. Guanter, G. Camps-Valls, J. Calpe, and J. Moreno, "Modelling spatial and spectral systematic noise patterns on CHRIS/PROBA hyperspectral data," *Proc. SPIE* **6365**, 63650Z (2006).
11. A. Theuwissen, *Solid-State Imaging with Charge-Coupled Devices* (Kluwer Academic, 1995).
12. M. Cutter, "Review of aspects associated with the CHRIS calibration," in "*Proceedings of the 2nd CHRIS/Proba Workshop*," ESA SP-578 (European Space Agency, 2004), paper 6_cutter.pdf.
13. S. N. Torres, J. E. Pezoa, and M. M. Hayat, "Scene-based nonuniformity correction for focal plane arrays by the method of the inverse covariance form," *Appl. Opt.* **42**, 5872–5881 (2003).
14. J. E. Pezoa, M. M. Hayat, S. N. Torres, and M. S. Rahman, "Multimodel Kalman filtering for adaptive nonuniformity correction in infrared sensors," *J. Opt. Soc. Am. A* **23**, 1282–1291 (2006).
15. F. Gadallah, F. Csillag, and E. Smith, "Destriping multisensor imagery with moment matching," *Int. J. Remote Sensing* **21**, 2505–2511 (2000).
16. J. Garcia and J. Moreno, "Removal of noises in CHRIS/Proba images: Application to the SPARC campaign data," in "*Proceedings of the 2nd CHRIS/Proba Workshop*," ESA SP-578 (European Space Agency, 2004), paper 9_GARCIA.pdf.
17. J. Settle and M. Cutter, "HDFclean V2. A program for reprocessing images captured by the CHRIS hyper-spectral imager" (2005), <http://earth.esa.int/proba/>.
18. P. Mlsna and T. Becker, "Striping artifact reduction in lunar orbiter mosaic images," in *2006 IEEE Southwest Symposium on Image Analysis and Interpretation* (IEEE Computer Society, 2006), pp. 95–99.
19. R. Leathers, T. Downes, and R. Priest, "Scene-based nonuniformity corrections for optical and SWIR pushbroom sensors," *Opt. Express* **13**, 5136–5150 (2005).
20. L. Gómez-Chova, J. Amorós, G. Camps-Valls, J. Martín, J. Calpe, L. Alonso, L. Guanter, J. Fortea, and J. Moreno, "Cloud detection for CHRIS/Proba hyperspectral images," *Proc. SPIE* **5979**, 59791Q (2005).
21. N. Fomferra and C. Brockmann, "BEAM—the ENVISAT MERIS and AATSR Toolbox," in "*Proceedings of the MERIS (A) ATSR Workshop 2005*," ESA SP-597 (European Space Agency, 2005), paper paper_Fomferra.pdf.
22. The BEAM Toolbox is a collection of open-source executable tools supported by ESA to facilitate the utilization, viewing, and processing of ESA Earth observation data. More information is available at <http://envisat.esa.int/resources/software/tools/> or <http://www.brockmann-consult.de/beam/>.
23. CHRIS products are provided in top of the atmosphere radiance in a HDF v4 file format, which includes additional acquisition information (image date, azimuth and zenith view angles, etc.) contained in the metadata attributes of the CHRIS HDF file [9].
24. L. Guanter, L. Alonso, and J. Moreno, "A method for the surface reflectance retrieval from PROBA/CHRIS data over land: application to ESA SPARC campaigns," *IEEE Trans. Geosci. Remote Sensing* **43**, 2908–2917 (2005).
25. M. Cutter and L. Johns, "CHRIS data format," SIRA Tech. Rep. Issue 4.2 (European Space Agency, 2005), document 271.DO.13, <http://earth.esa.int/proba/>.
26. R. Larsen, A. A. Nielsen, and K. Conradsen, "Restoration of hyperspectral push-broom scanner data," in *Proceedings of the 17th EARSeL Symposium on Future Trends in Remote Sensing*, P. Gudmandsen, ed. (A. A. Balkema, 1998), pp. 157–162.
27. W. K. Pratt, *Digital Image Processing: PIKS Inside*, 3rd ed. (Wiley, 2001).
28. N. Keshava, "Distance metrics and band selection in hyperspectral processing with applications to material identification and spectral libraries," *IEEE Trans. Geosci. Remote Sensing* **42**, 1552–1565 (2004).
29. H. Othman and S.-E. Qian, "Noise reduction of hyperspectral imagery using hybrid spatial-spectral derivative-domain wavelet shrinkage," *IEEE Trans. Geosci. Remote Sensing* **44**, 397–408 (2006).
30. L. L. Lapin, *Probability and Statistics for Modern Engineering* (Duxbury, PWS Publishers, 1983).

ISSN: 0003-6935

Applied Optics

Multispectral
and
Hyperspectral
Imaging



OSA[®]
The Optical Society

1 October 2008

